Supplementary Information

4*f*-5*d* orbital tag-team catalysis empowers high-loading zinc–iodine batteries

Maoxin Chen[1,2,3,4,#], Yuanyuan He[4,#], Huan Li[5,#], Zhitan Wu[1,2,4], Jinxing Chen[4], Ao Du[1], Li Wang[1,3], Jiong Lu[4], Weichao Wang[5✉], Chunpeng Yang[1,3✉], Quan-Hong Yang[1,2,3✉]

[1]Nanoyang Group, Tianjin Key Laboratory of Advanced Carbon and Electrochemical Energy Storage, School of Chemical Engineering and Technology, and Collaborative Innovation Center of Chemical Science and Engineering (Tianjin), Tianjin University, Tianjin 300350, China

[2]Joint School of National University of Singapore and Tianjin University, International Campus of Tianjin University, Binhai New City, Fuzhou 350207, China

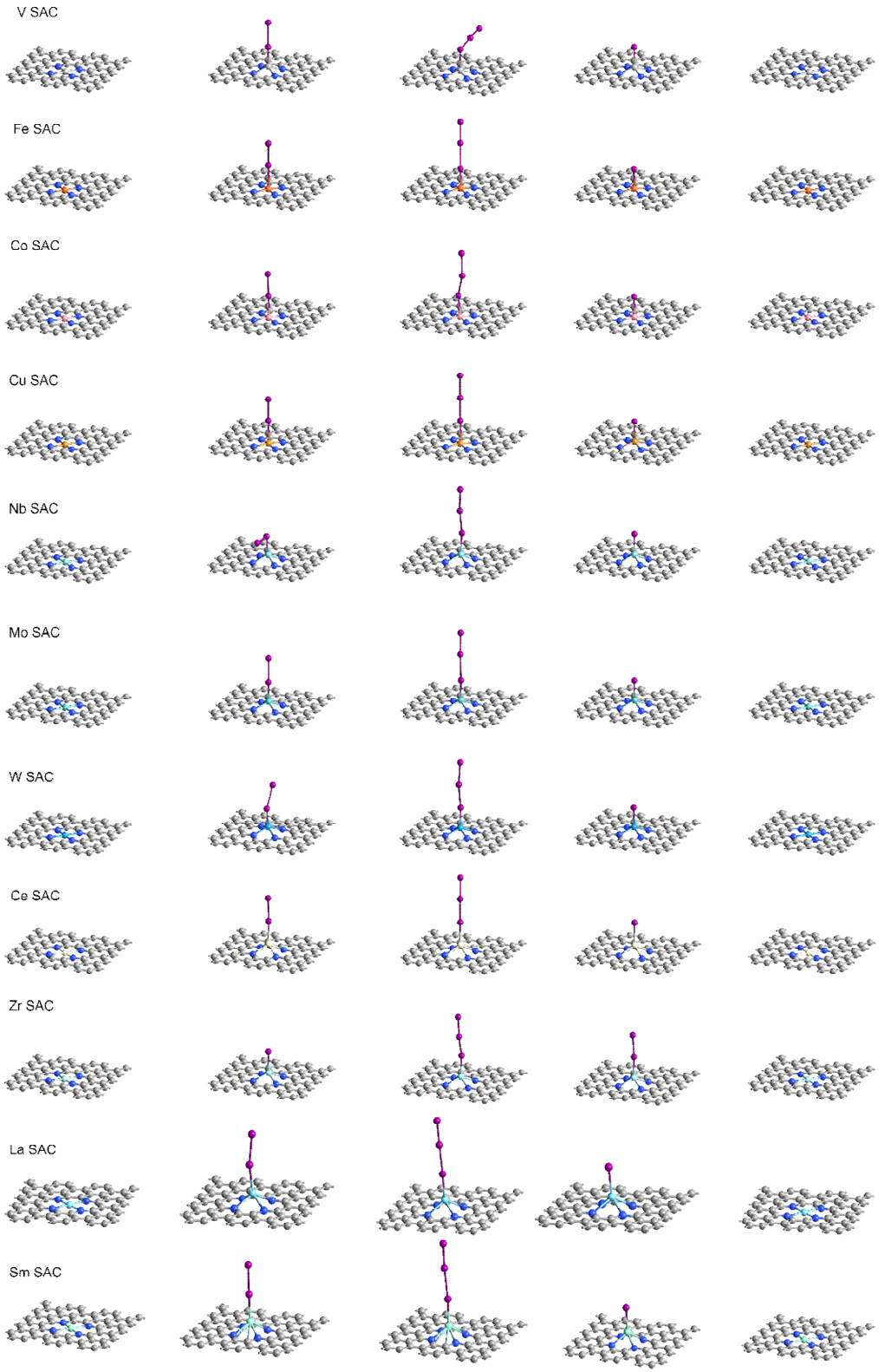
[3]Haihe Laboratory of Sustainable Chemical Transformations, Tianjin 300192, China

[4]Department of Chemistry, National University of Singapore, 3 Science Drive 3, Singapore 117543, Singapore

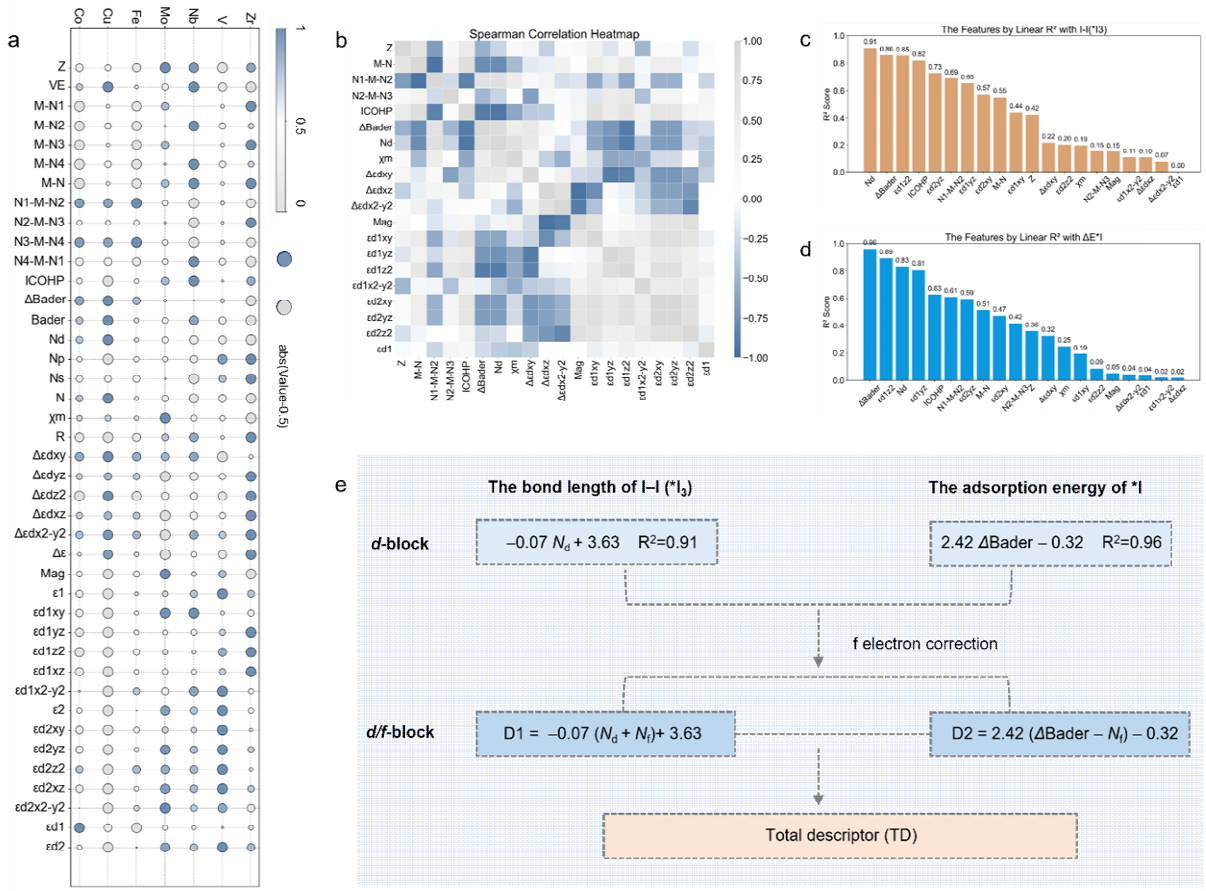
[5]College of Electronic Information and Optical Engineering, Nankai University, Tianjin 300071, China

[#]These authors contributed equally to this work.

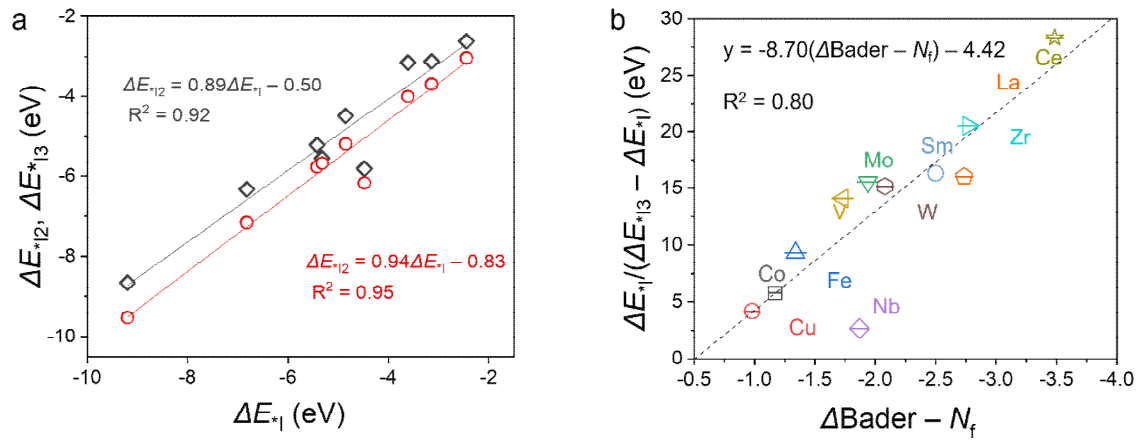
[✉]E-mail: weichaowang@nankai.edu.cn; cpyang@tju.edu.cn; qhyangcn@tju.edu.cn



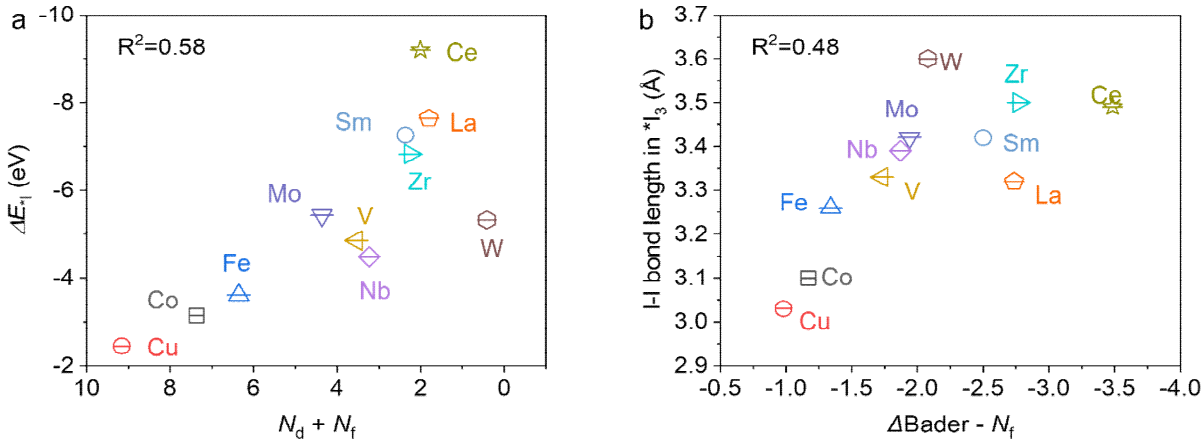
Supplementary Fig. 1 | Optimized adsorption configurations of iodine species on various SACs. The image shows eleven SAC samples, arranged from top to bottom as follows: V SAC, Fe SAC, Co SAC, Cu SAC, Nb SAC, Mo SAC, W SAC, Ce SAC, Zr SAC, La SAC and Sm SAC. Source data are provided as a Source Data file.



Supplementary Fig. 2 | Feature analysis and descriptor identification for SACs. a, Feature importance analysis across different metal-ligand systems. **b,** Spearman correlation heatmap illustrating inter-feature relationships. **c–d,** Ranking of key features based on their linear correlation (R^2) with I–I bond length (c) and *I adsorption energy (d). **e,** Descriptor construction workflow. Source data are provided as a Source Data file.



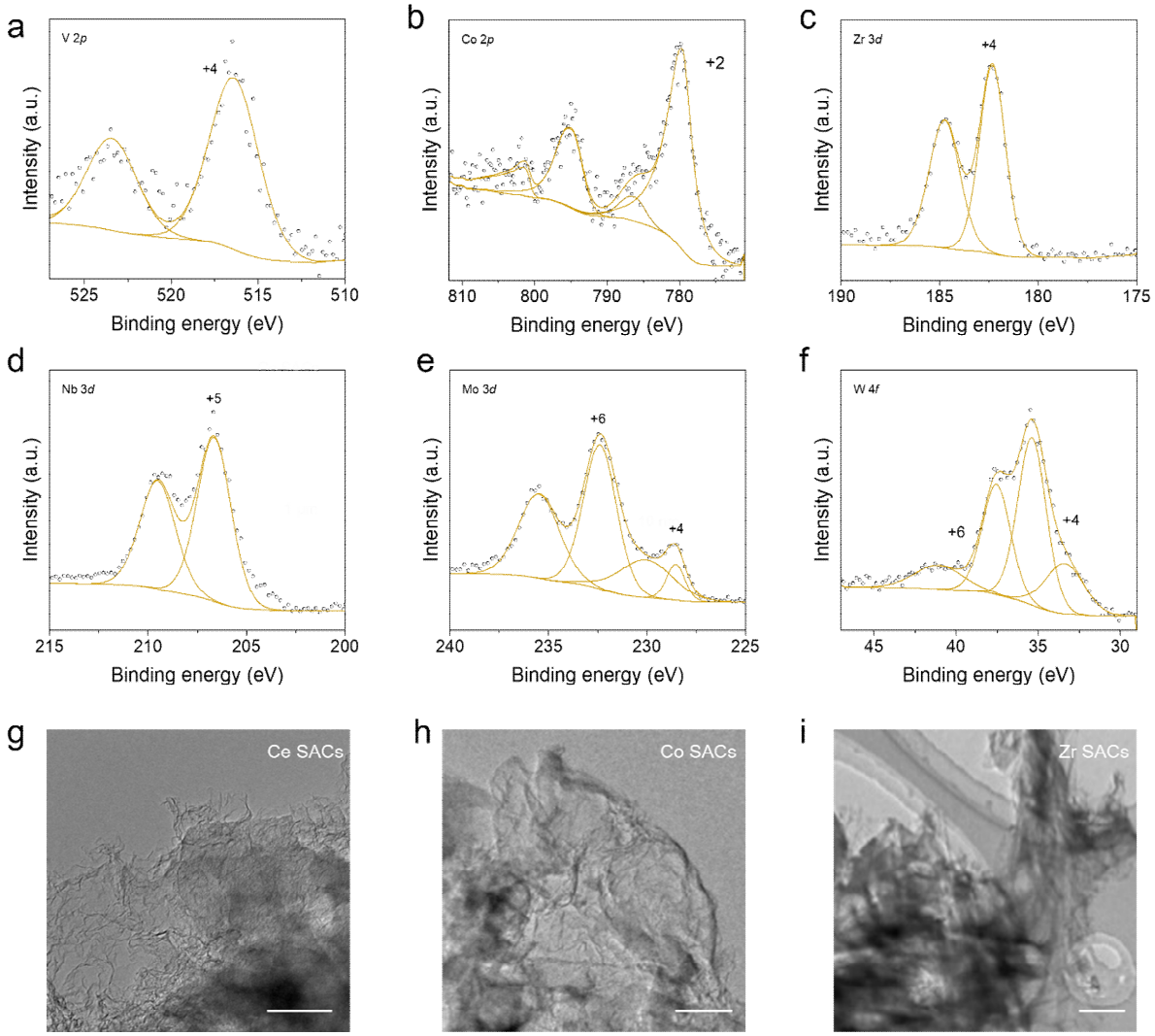
Supplementary Fig. 3 | Adsorption energy correlations among iodine species. a, The linear relationship among the adsorption energies of the three iodine species. **b,** The adsorption energy preference between *I and *I_3.



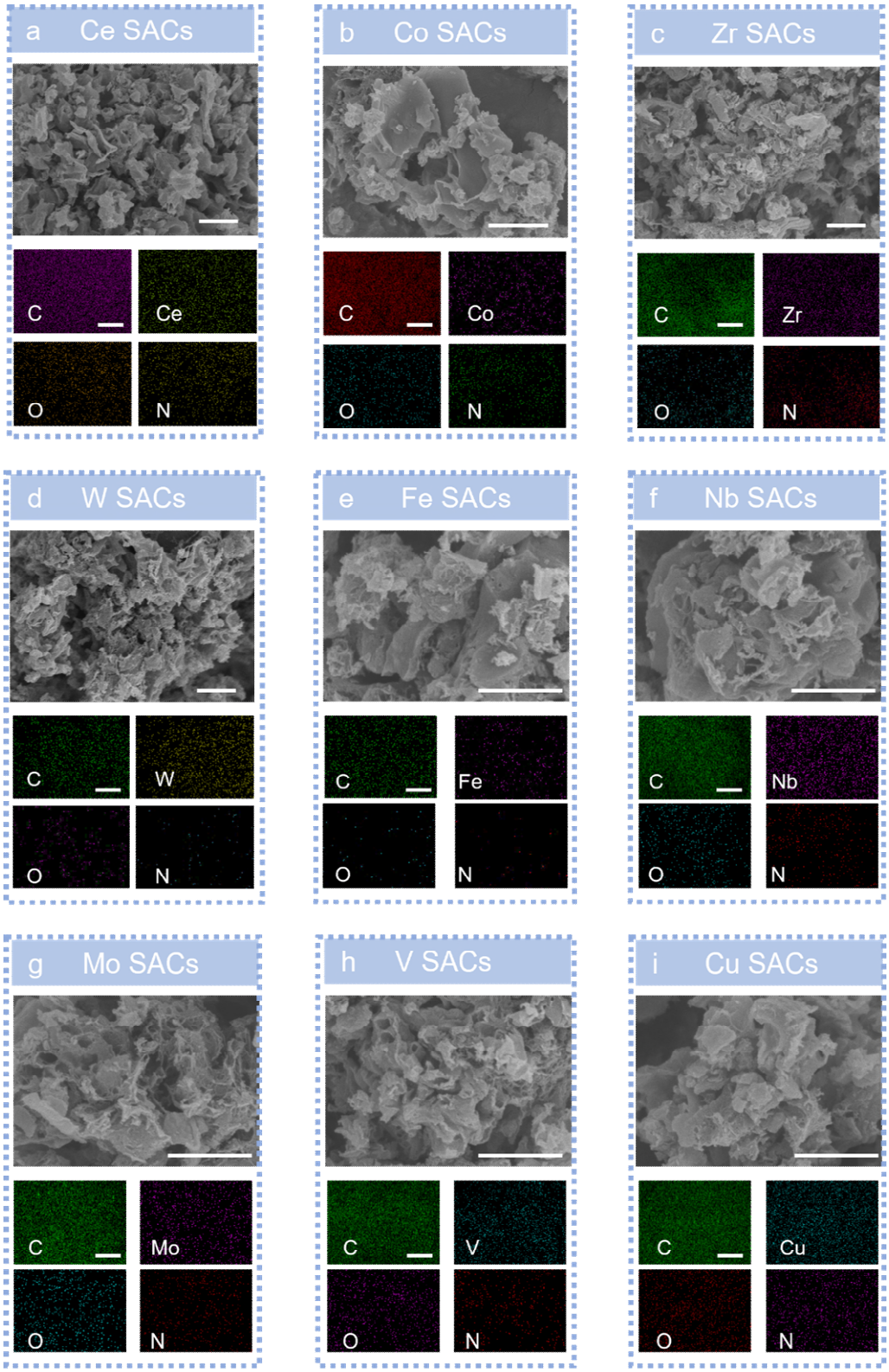
Supplementary Fig. 4 | Descriptor correlations with adsorption and bond activation. a, Correlation between the adsorption energy of I^- (ΔE_{*I}) and N_d + N_f for different SACs. **b,** Correlation between the I–I bond length in *I_3 and ΔBader – N_f for different SACs. Source data are provided as a Source Data file.

N_d+N_f (total *d/f* electron count) is the primary descriptor for the I-I bond activation step, showing a strong correlation with the I–I bond length (R^2=0.81) but a much weaker one with adsorption energy (R^2=0.58).

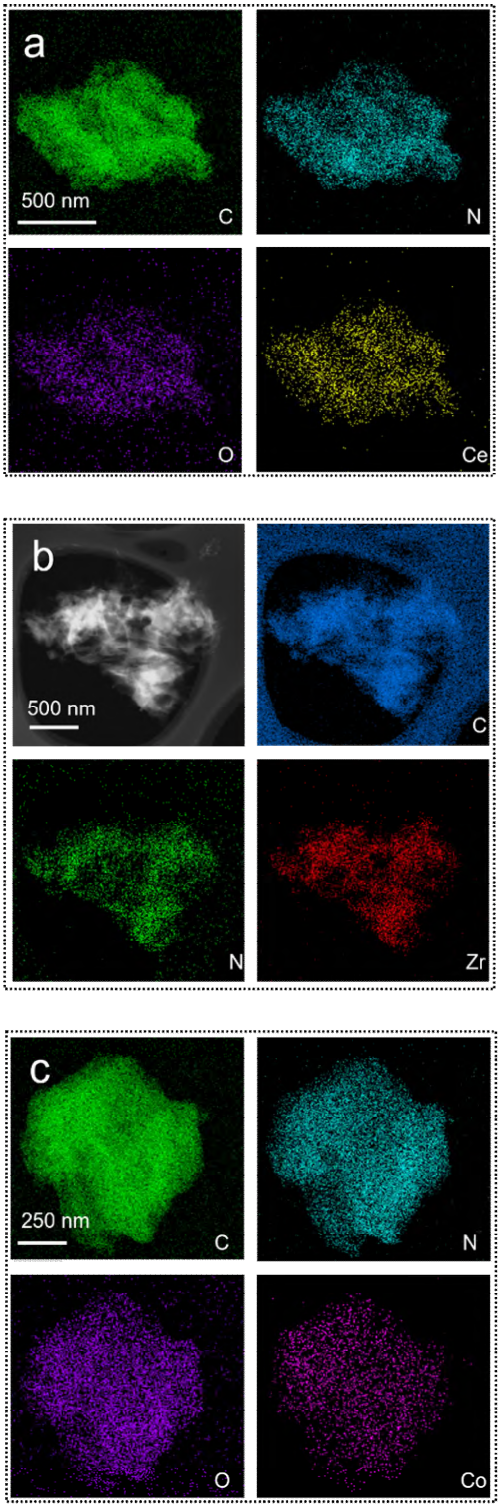
Conversely, ΔBader – N_f (metal-ligand charge polarization) is the dominant descriptor for the adsorption step, strongly predicting adsorption energy (ΔE*I, R^2=0.89) while poorly predicting the I–I bond length (R^2=0.48).



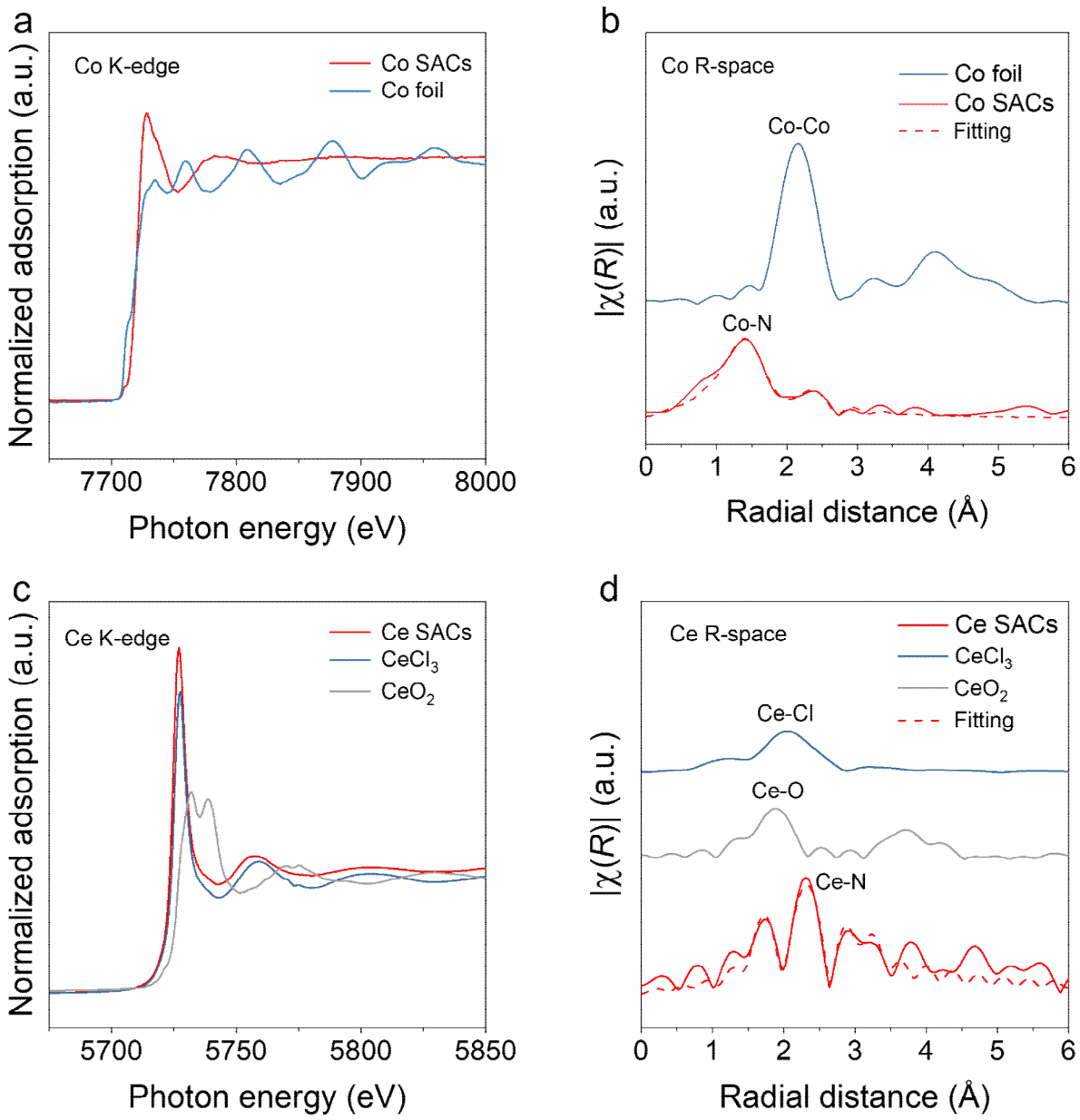
Supplementary Fig. 5 | XPS and TEM characterization of the as-prepared SACs. a–f, XPS spectra of V 2*p*, Co 2*p*, Zr 3*d*, Nb 3*d*, Mo 3*d* and W 4*f* for the corresponding SACs. **g–i**, TEM images of Ce SACs, Zr SACs and Co SACs (scale bars: 300 nm). Source data are provided as a Source Data file.



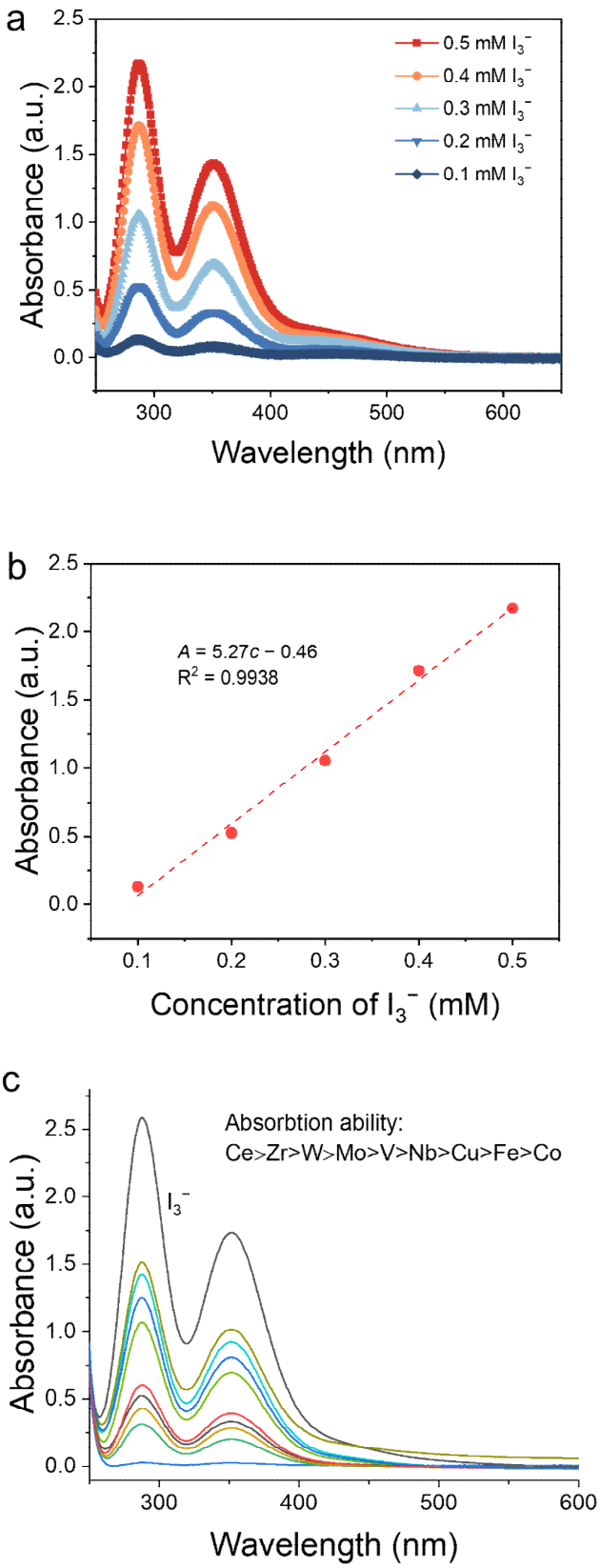
Supplementary Fig. 6 | Morphological and elemental characterization of the as-prepared SACs via SEM and EDS mappings. a–i, Ce SACs, Co SACs, Zr SACs, W SACs, Fe SACs, Nb SACs, Mo SACs, V SACs and Cu SACs. Scale bars: 500 nm.



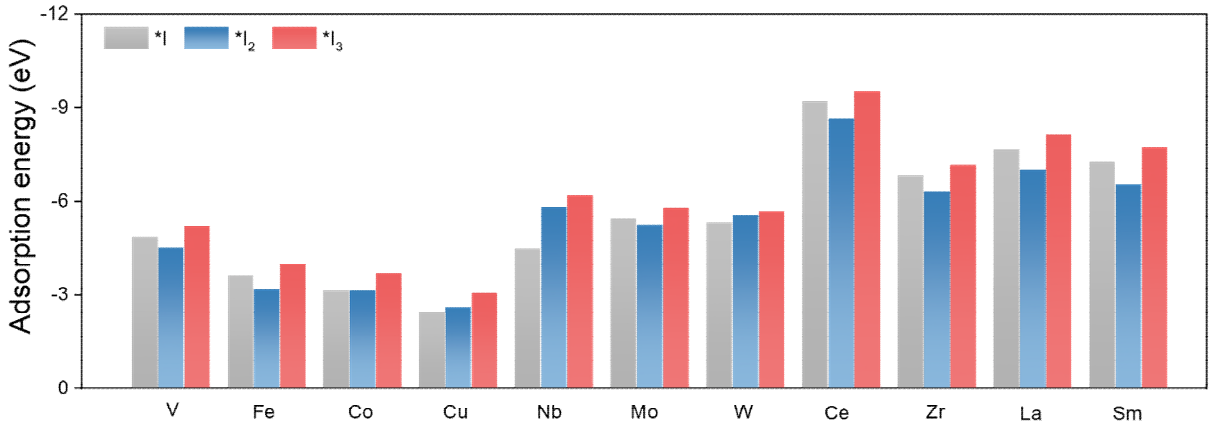
Supplementary Fig. 7 | TEM elemental mappings of Ce, Zr, and Co SACs. a, TEM elemental mappings of Ce SAC. **b**, TEM image and elemental mappings of Zr SAC. **c**, TEM elemental mappings of Co SAC.



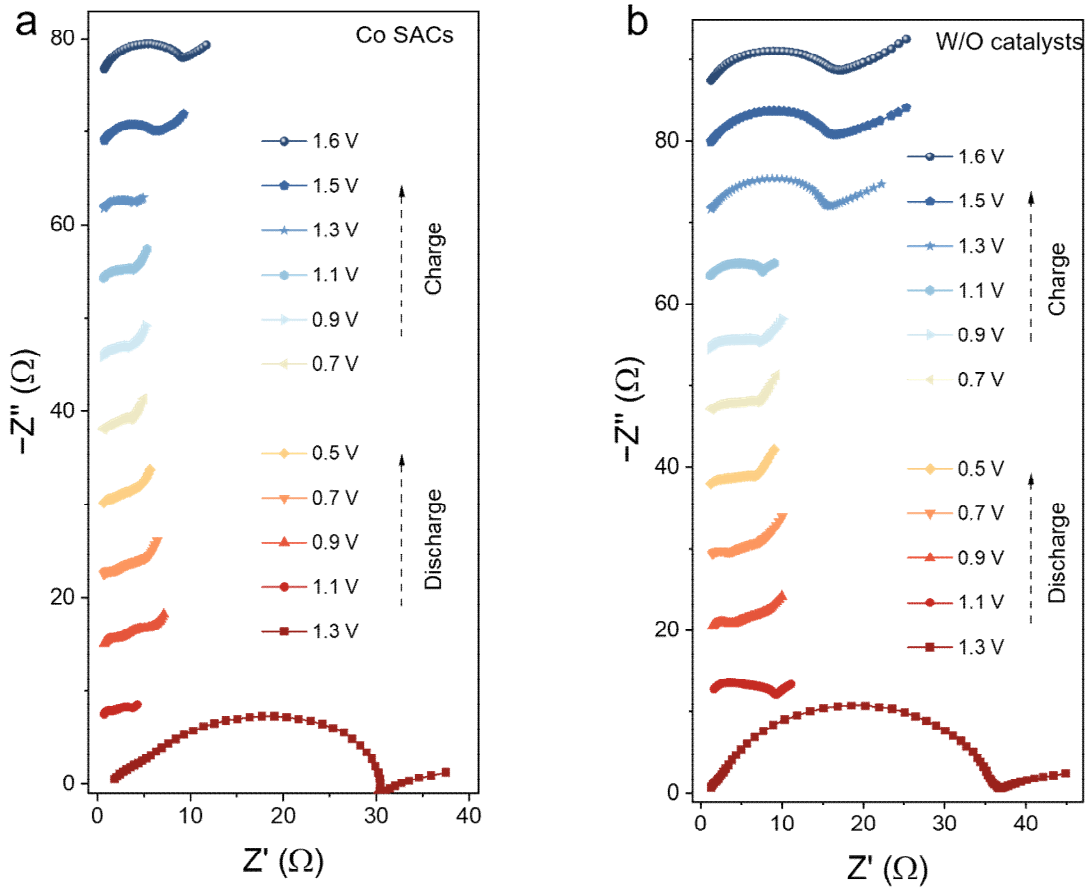
Supplementary Fig. 8 | Synchrotron radiation analysis of Co and Ce SACs. **a, c,** X-ray absorption near-edge structure (XANES) spectra for Co and Ce SACs, respectively. **b, d,** Extended X-ray absorption fine structure (EXAFS) spectra for Co and Ce SACs, respectively. Source data are provided as a Source Data file.



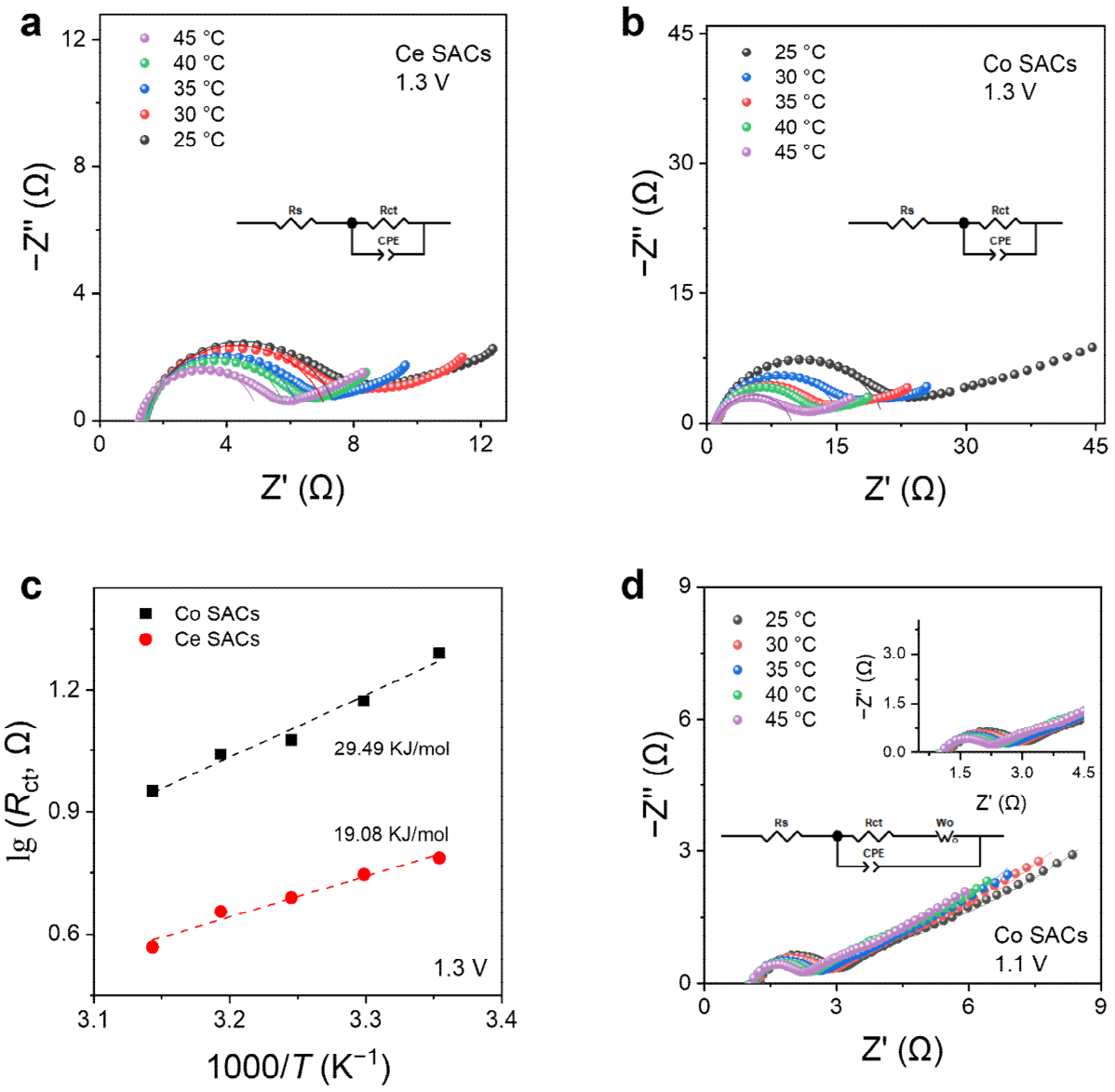
Supplementary Fig. 9 | UV-Vis absorption analysis of I_3^- adsorption by SACs. a, UV-Vis absorption spectra of the standard solution. **b,** The standard calibration curve of I_3^- concentration. **c,** UV–vis absorption spectra of polyiodide solutions treated with different SACs for 24 hours. Source data are provided as a Source Data file.



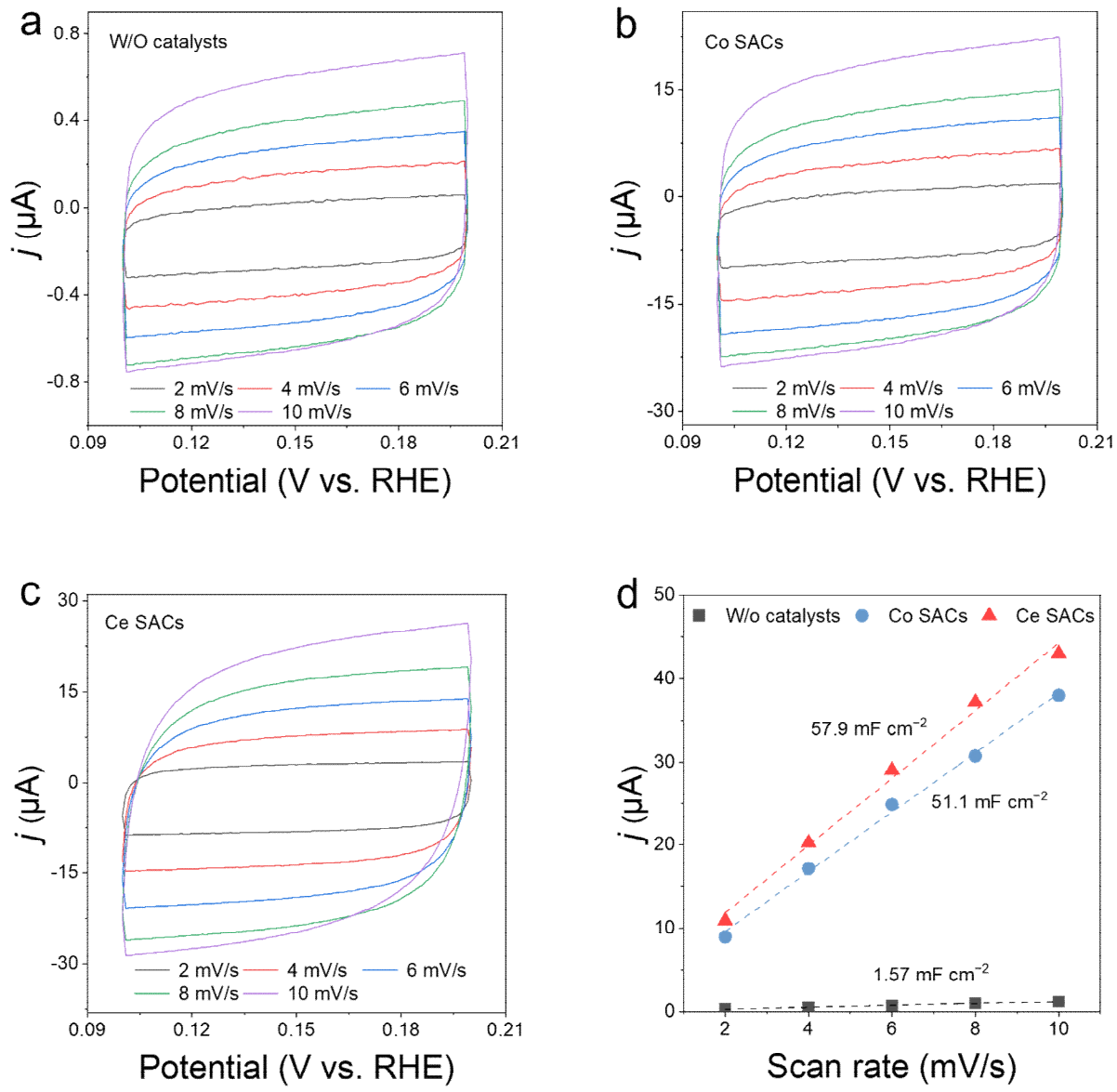
Supplementary Fig. 10 | Adsorption energy comparison for *I, *I_2, and *I_3 on different SACs. The adsorption energies of *I, *I_2, and *I_3 on various single-atom catalysts with metal centers M = V, Fe, Co, Cu, Nb, Mo, W, Ce, La, and Sm are displayed. Source data are provided as a Source Data file.



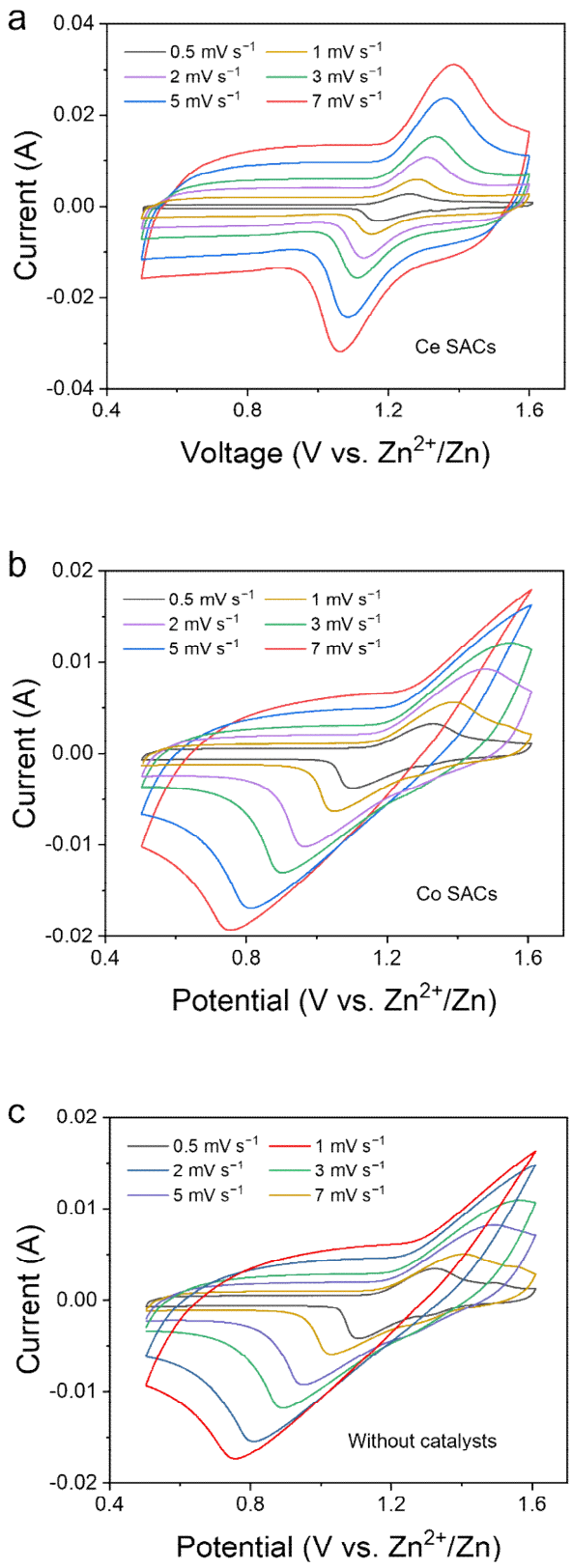
Supplementary Fig. 11 | *In situ* electrochemical impedance spectroscopy of Co SACs and catalyst-free electrodes. a, b, Nyquist plots for Co SACs (a) and catalyst–free electrodes (b) at varying potentials (vs. Zn^{2+}/Zn). Source data are provided as a Source Data file.



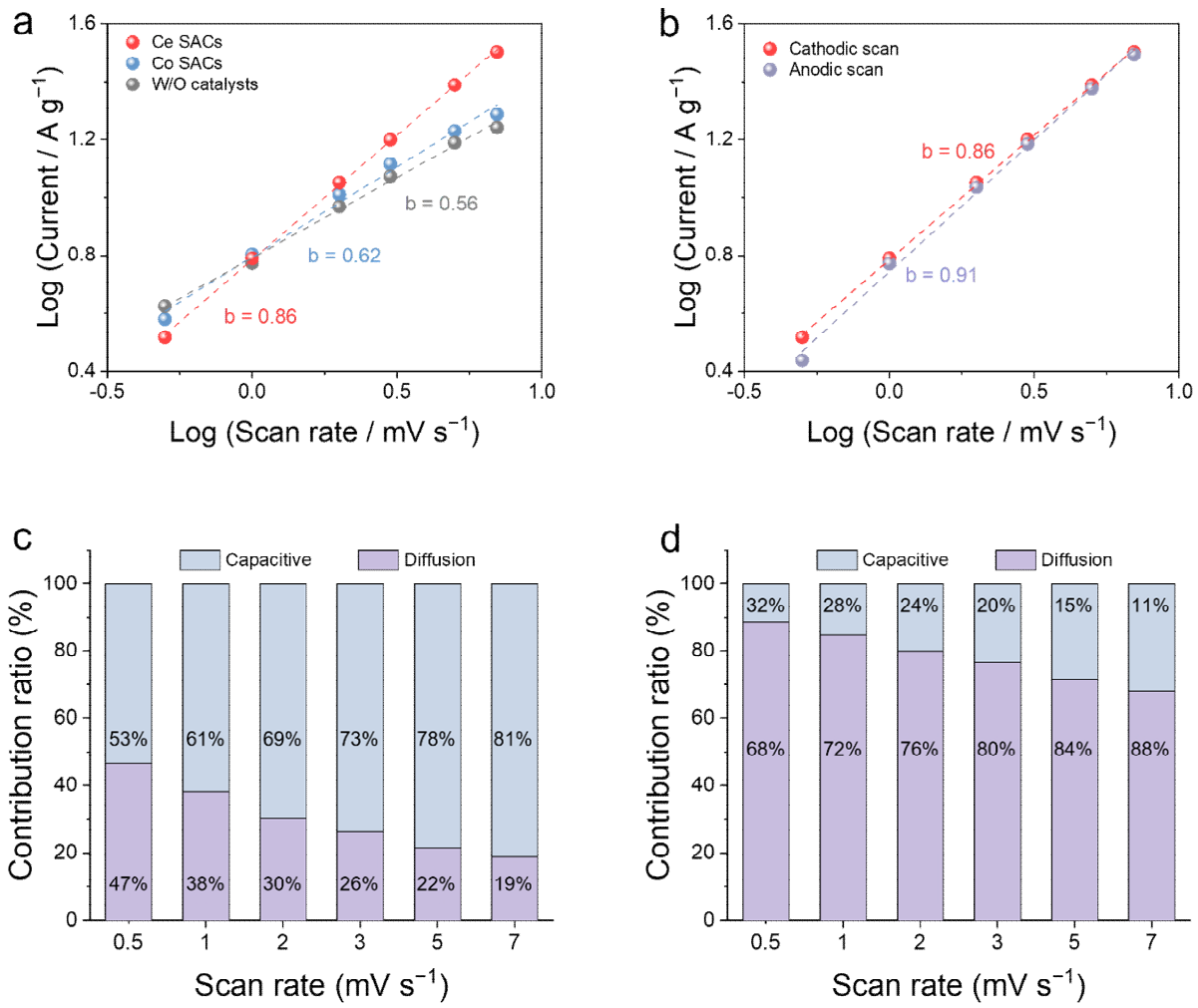
Supplementary Fig. 12 | Temperature-dependent electrochemical impedance and activation energy analysis. a, **b**, Nyquist plots of Ce SACs (a) and Co SACs (b) at 1.3 V vs. Zn^{2+}/Zn under varying temperatures (25–45 °C). **c**, Arrhenius plots derived from EIS data at 1.3 V. **d**, Nyquist plots of Co SACs at 1.1 V vs. Zn^{2+}/Zn under varying temperatures (25–45 °C). Source data are provided as a Source Data file.



Supplementary Fig. 13 | ECSA analysis. a–c, ECSA evaluation for W/O catalysts (a), Co SACs (b) and Ce SACs (c) via cyclic voltammetry (CV) in a non-faradaic potential window (0.1–0.2 V vs. Zn^{2+}/Zn) at scan rates of 10–100 mV s^{-1}. **d**, Linear regression of capacitive current versus scan rate (slope = double−layer capacitance, C_{dl}), used to calculate ECSA. All tests were conducted in 2 M $ZnSO_4$ electrolyte. Source data are provided as a Source Data file.

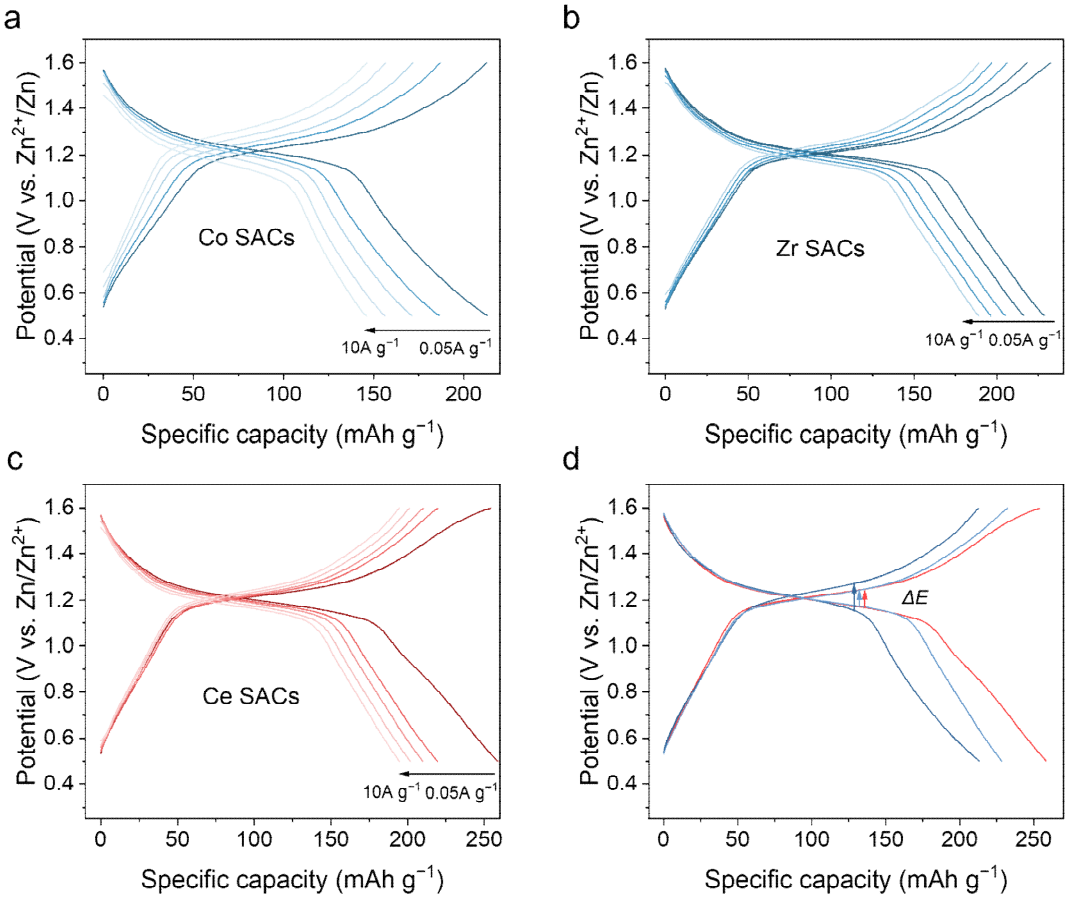


Supplementary Fig. 14 | Scan rate-dependent cyclic voltammetry of different electrodes. a–c, Scan rate-dependent CV curves of Co SACs (a), Co SACs (b) and without catalysts. Source data are provided as a Source Data file.

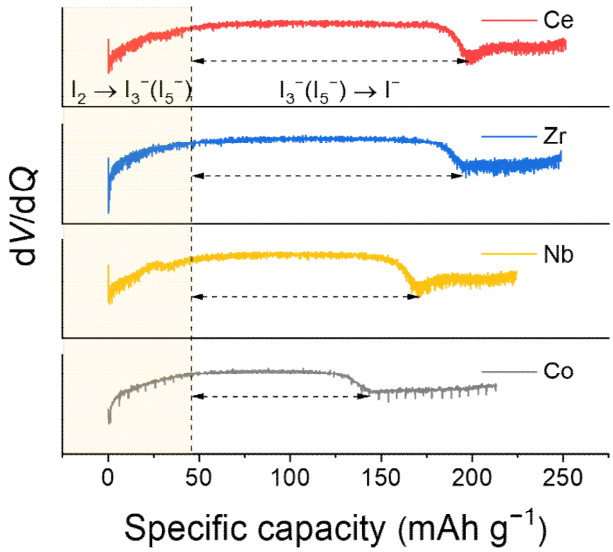


Supplementary Fig. 15 | Kinetic analysis of iodine conversion on different electrodes. a, Log*i* versus logν plots of the cathodic current response for Ce SACs/I_2, Co SACs/I_2 and W/O catalysts electrodes. **b,** Log*i* versus logν plots of the cathodic and anodic current response for Ce SACs/I_2 electrodes. **c**, **d**, The diffusion and capacitive contributions of iodine conversion with Ce SACs (c) and Co SACs (d) under different scan rates. Source data are provided as a Source Data file.

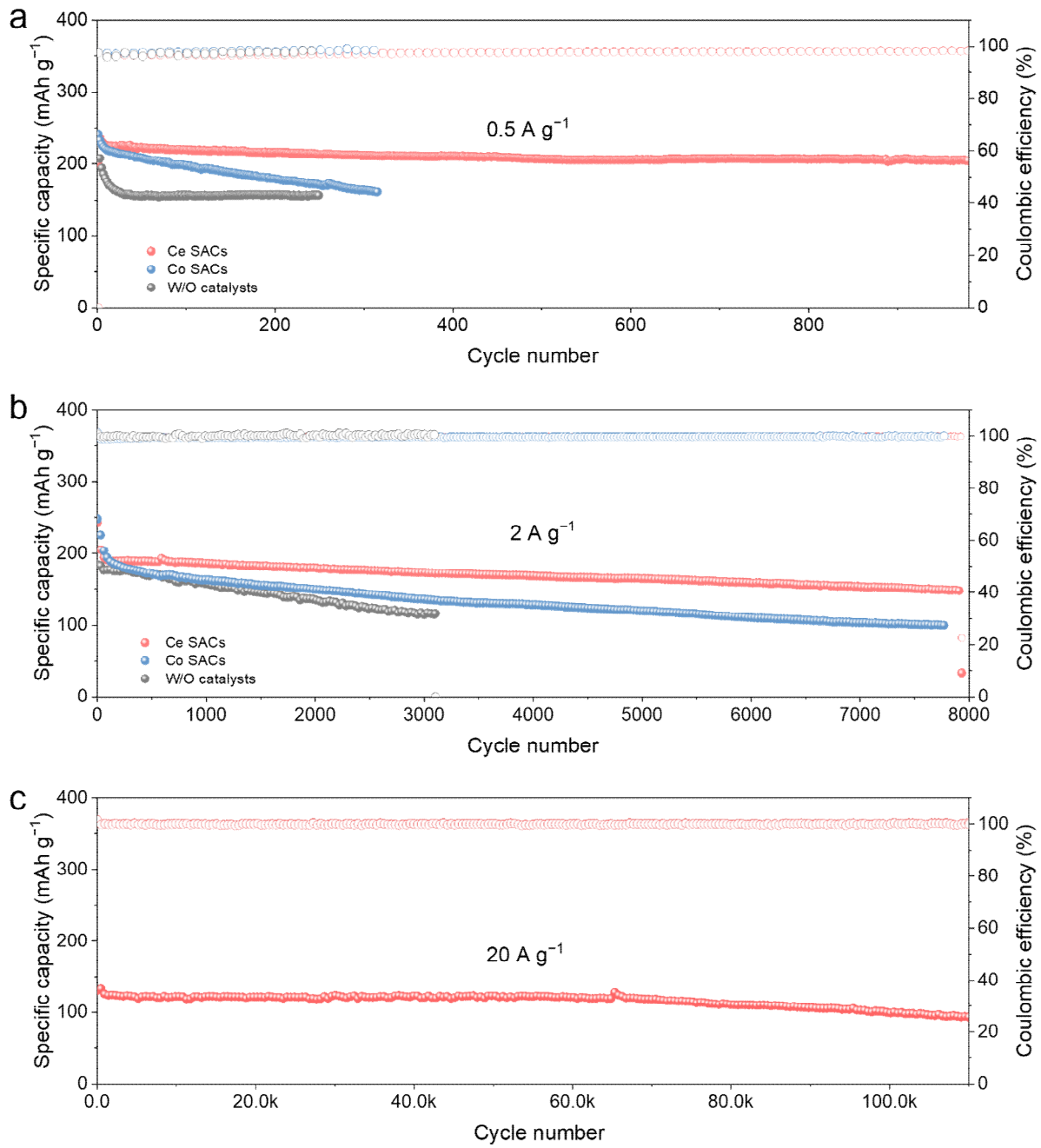
Kinetic analysis via the power-law relationship ($I = a\nu^b$) identifies surface capacitive dominance for Ce SACs, with *b*–values of 0.86 (Peak A) and 0.91 (Peak B), contrasting sharply with diffusion-limited behavior (*b* near to 0.5) in catalyst-free systems (Supplement Fig. 13a, b). Quantitative deconvolution ($i/\nu^{1/2} = k_1\nu + k_2\nu^{1/2}$) further confirms that Ce SACs achieve a capacitive contribution of 53% at 0.5 mV s^{-1}, higher than that of catalyst–free electrodes (32%), consistent with their superior rate capability across all tested scan rates (Supplement Fig. 13c, d).



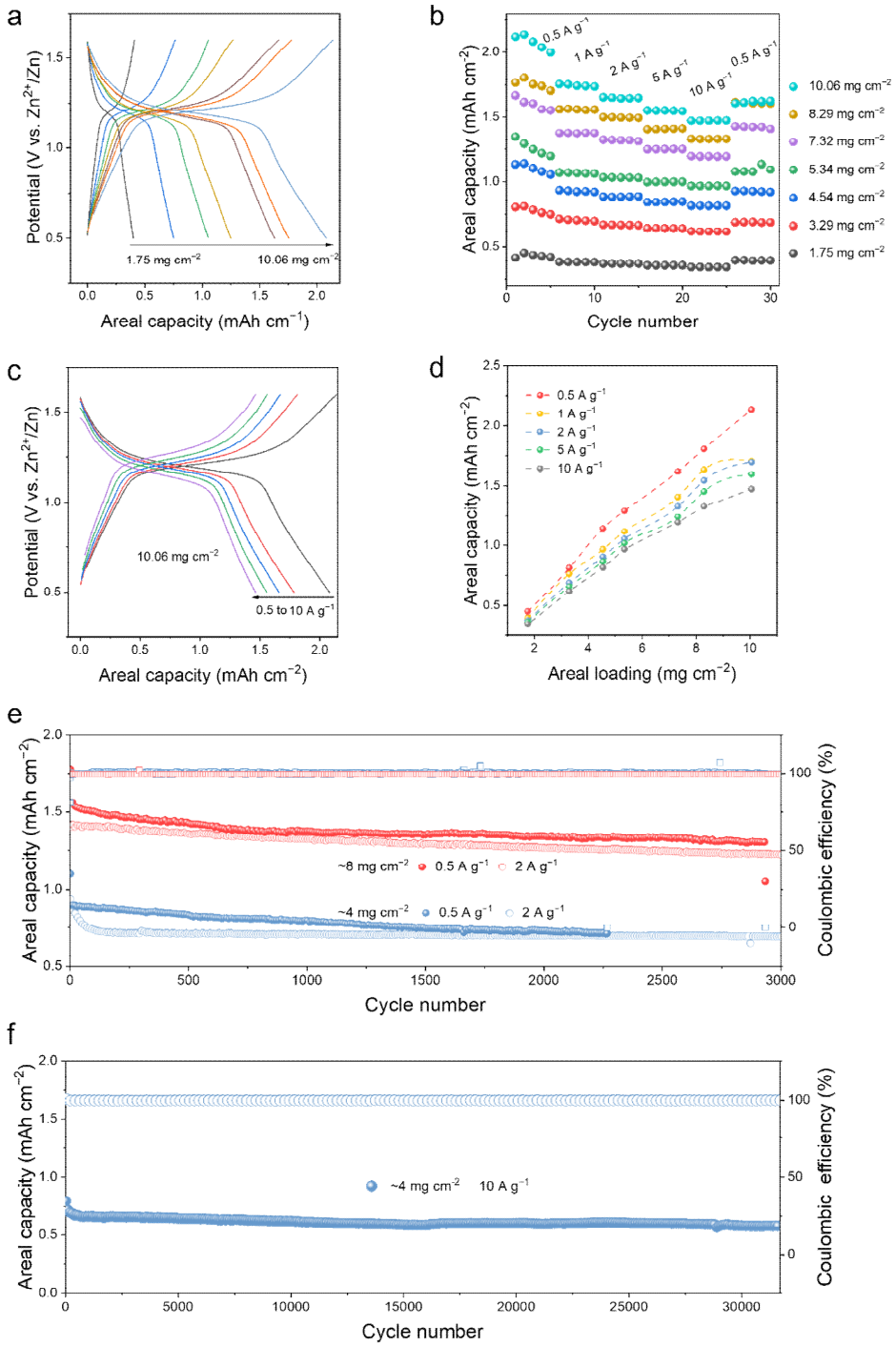
Supplementary Fig. 16 | Rate performance and polarization analysis of SAC-based cathodes. a–c, Galvanostatic charge–discharge profiles of iodine positive electrodes with Co SACs (a), Zr SACs (b) and Ce SACs (c) at varying specific current. **d**, Polarization analysis at 0.5 A g^{-1}. Source data are provided as a Source Data file.



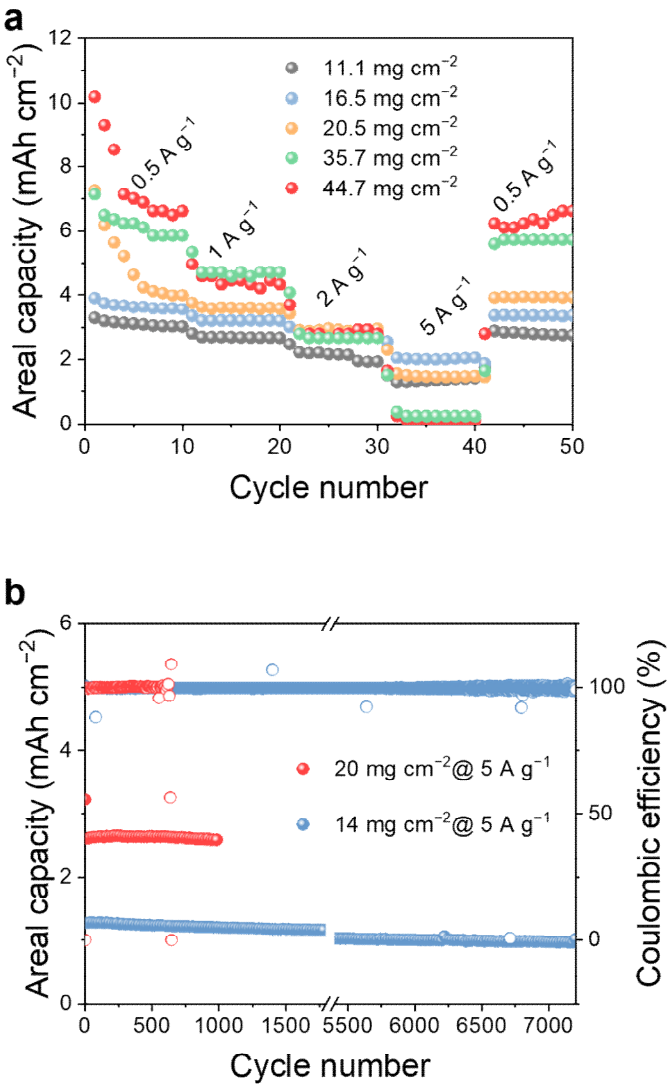
Supplementary Fig. 17 | Inverse differential capacity (d*V*/d*Q*) curves of Zn||I_2 batteries with different SAC-based cathodes. The d*V*/d*Q* curves are shown for Ce SACs/I_2, Zr SACs/I_2, Nb SACs/I_2, and Co SACs/I_2 cathodes, derived from the galvanostatic charge-discharge profiles at 0.5 A g^{-1}. Source data are provided as a Source Data file.



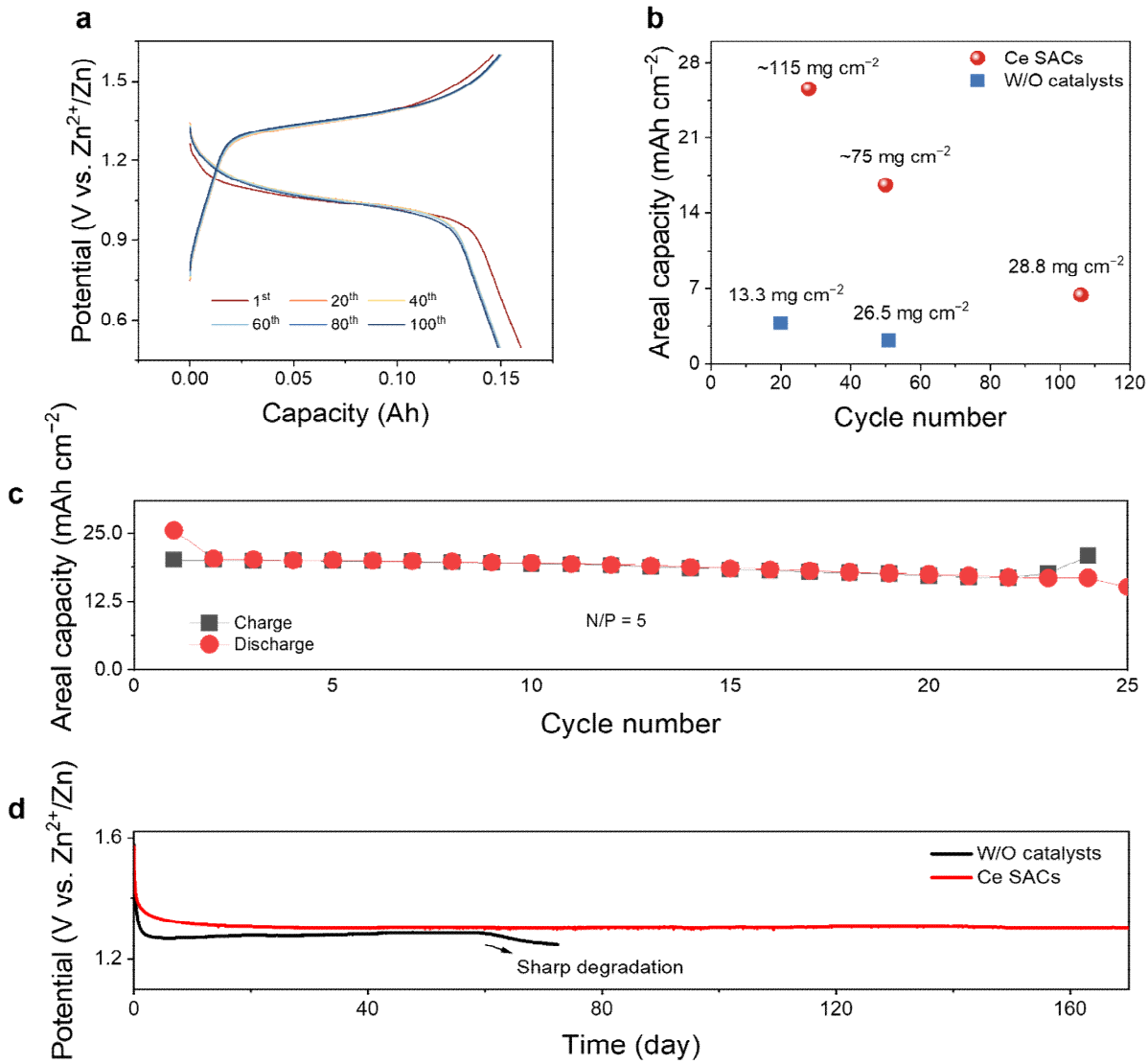
Supplementary Fig. 18 | Long-term cycling stability of Zn||I_2 batteries with different cathodes. a−c, Long-term cycling stability at 0.5 A g^{-1} (a), 2 A g^{-1} (b) and 20A g^{-1} (c). Source data are provided as a Source Data file.



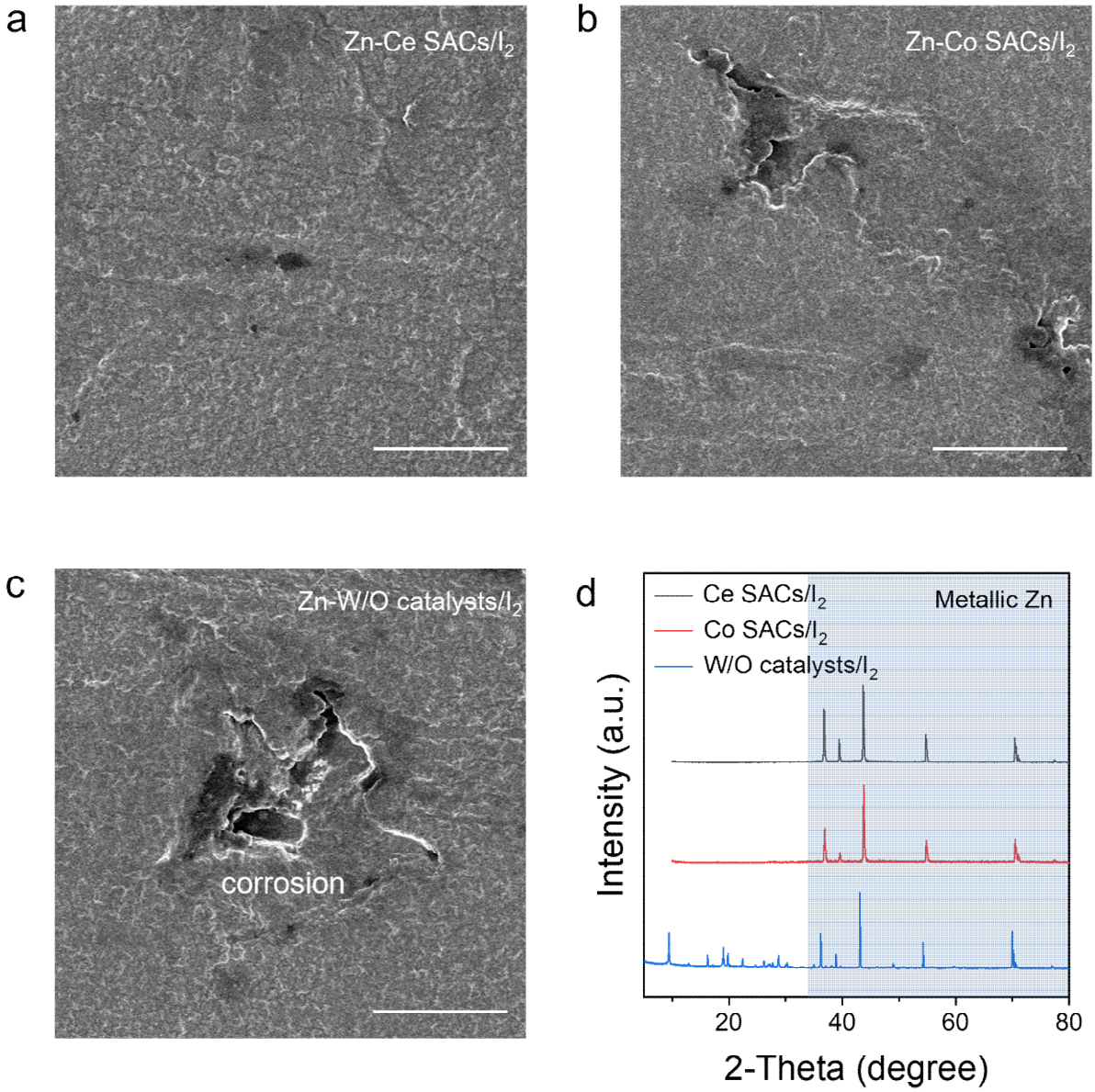
Supplementary Fig. 19 | Electrochemical performance of Ce SACs/I_2 electrodes a, Galvanostatic charge–discharge profiles at 0.5 A g^{-1} with areal loadings ranging from 1.75 to 10.06 mg cm^{-2}. **b**, Rate performance across loadings from 1.75 to 10.06 mg cm^{-2} from 0.5 to 10 A g^{-1}. **c**, Galvanostatic charge–discharge curves at 10.06 mg cm^{-2} under specific current from 0.5 to 10 A g^{-1}. **d**, Areal capacity and areal loading of Ce SACs/I_2 electrodes across varying specific current (0.5–5 A g^{-1}). **e,** cycling stability and Coulombic efficiency of the electrode at a moderate mass loading of 4 mg cm^{-2} under various specific current (0.5, 2, and 10 A g^{-1}). **f,** The areal capacity retention over 30,000 cycles at a high specific current of 10 A g^{-1} and a mass loading of 4 mg cm^{-2}. Source data are provided as a Source Data file.



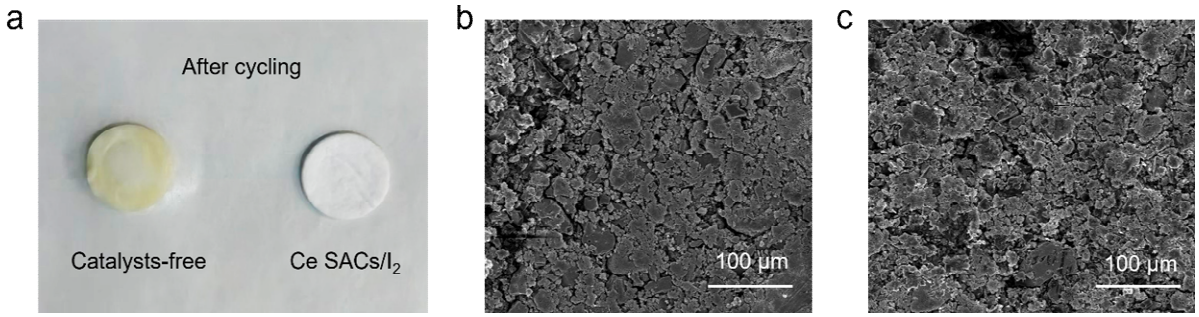
Supplementary Fig. 20 | Electrochemical performance of Ce SACs/I_2 cathodes under high mass loading conditions. a, rate capability at 11.1–44.7 mg cm^{-2} under specific current ranging from 0.5 to 5 A g^{-1}. **b,** cycling stability at 14 and 20 mg cm^{-2} under 5 A g^{-1}. Source data are provided as a Source Data file.



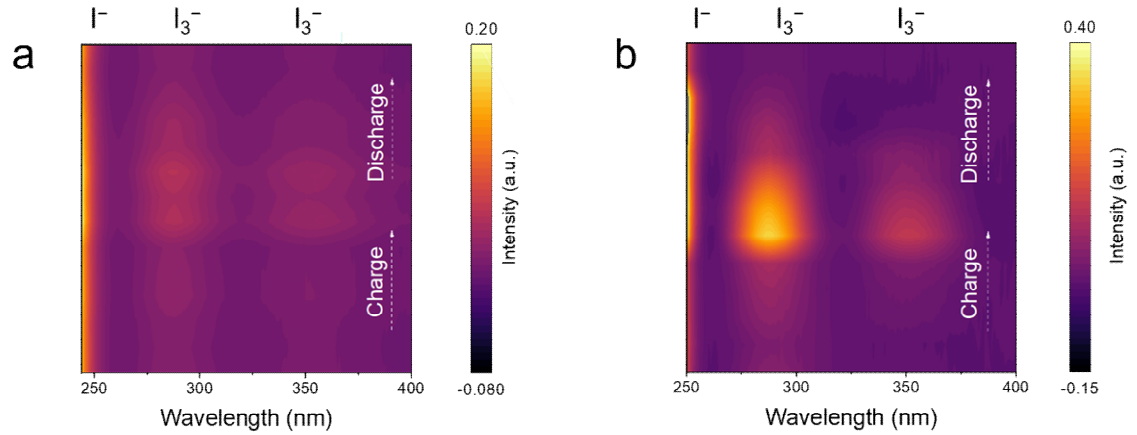
Supplementary Fig. 21 | Pouch cell performance and self-discharge behavior. a, Charge-discharge profiles at 0.36 A cm^{-2} for a Ce SACs/I_2 electrode with 28.8 mg cm^{-2}. **b** Comparison of areal capacity and cycle retention for electrodes with/without catalysts across different loadings. **c**, High-loading cycling performance (115 mg cm^{-2}) at 0.5 A g^{-1} (4×4 cm^2). **d,** Self-discharge tests for a Ce SACs/I_2 electrode versus catalyst-free electrodes. Source data are provided as a Source Data file.



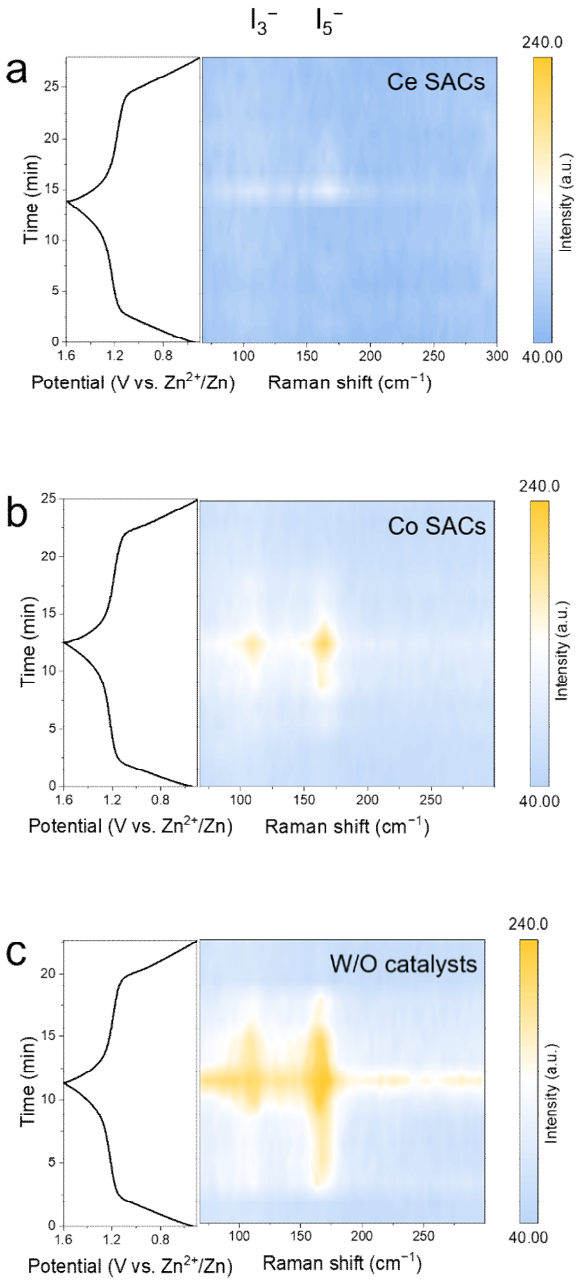
Supplementary Fig. 22 | Post-cycling characterization of zinc anodes. a–c, SEM images of Zn anodes after 50 cycles at 2 A g^{-1} in Ce SACs/I_2 (a), Co SACs/I_2 (b) and w/o catalysts/I_2 (c) (scale bars: 5 μm). **d,** XRD patterns of the cycled Zn electrodes in batteries. Source data are provided as a Source Data file.



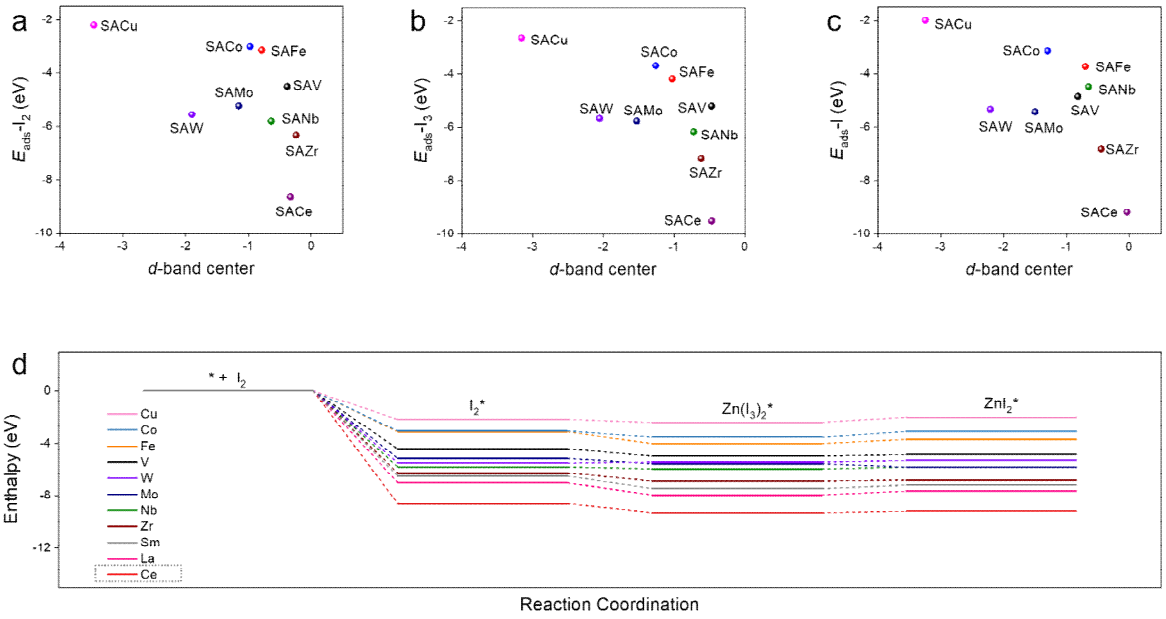
Supplementary Fig. 23 | Post-cycling analysis of separators and Ce SACs/I_2 cathodes. a, Optical images of separators disassembled from cells with Ce SACs/I_2 and catalyst-free electrodes. **b, c,** SEM images of the Ce SACs/I_2 positive electrode (a) before cycling and (b) after 100 cycles at 2 A g^{-1}.



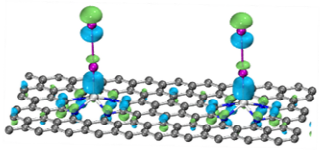
Supplementary Fig. 24 | *In situ* UV-Vis spectroscopy during electrochemical cycling. a, **b**, *In situ* UV–vis spectra during charge/discharge period at 4 mA for Ce SACs (a) and Co SACs (b). Source data are provided as a Source Data file.



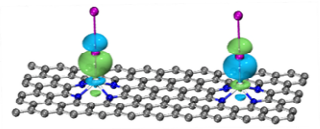
Supplementary Fig. 25 | *In situ* Raman spectroscopy during electrochemical cycling. a–c, *In situ* Raman spectra during cycling at 2 mA for, Ce SACs (a), Co SACs (b) and Catalyst–free electrodes (c). Source data are provided as a Source Data file.



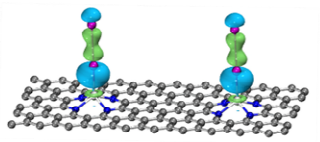
Supplementary Fig. 26 | DFT-based adsorption energy correlations and reaction enthalpy profiles. a–c, The relationship between the d-band center of different SACs and the adsorption energies for I_2* (a), I_3* (b) and I* (c) species. **d,** Enthalpy diagram for the I_2 reduction reaction on SACs. Source data are provided as a Source Data file.



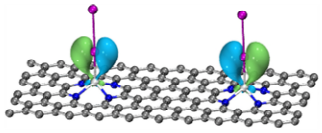
NAdO (1) = 0.796
-4.758 eV
Ce *f*: 0.195%; *d*: 5.870%



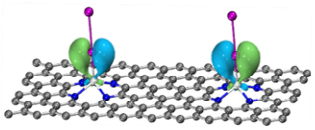
NAdO (2). = 0698
-7.566 eV
Ce *f*: 0.785%; *d*: 7.738%



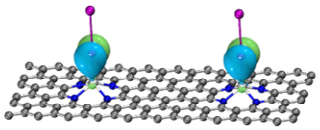
NAdO (3) = 0.564
-8.006 eV
Ce *f*: 0.462%; *d*: 4.269%



NAdO (4) = 0.473
-5.262 eV
Ce *f*: 1.313%; *d*: 2.898%

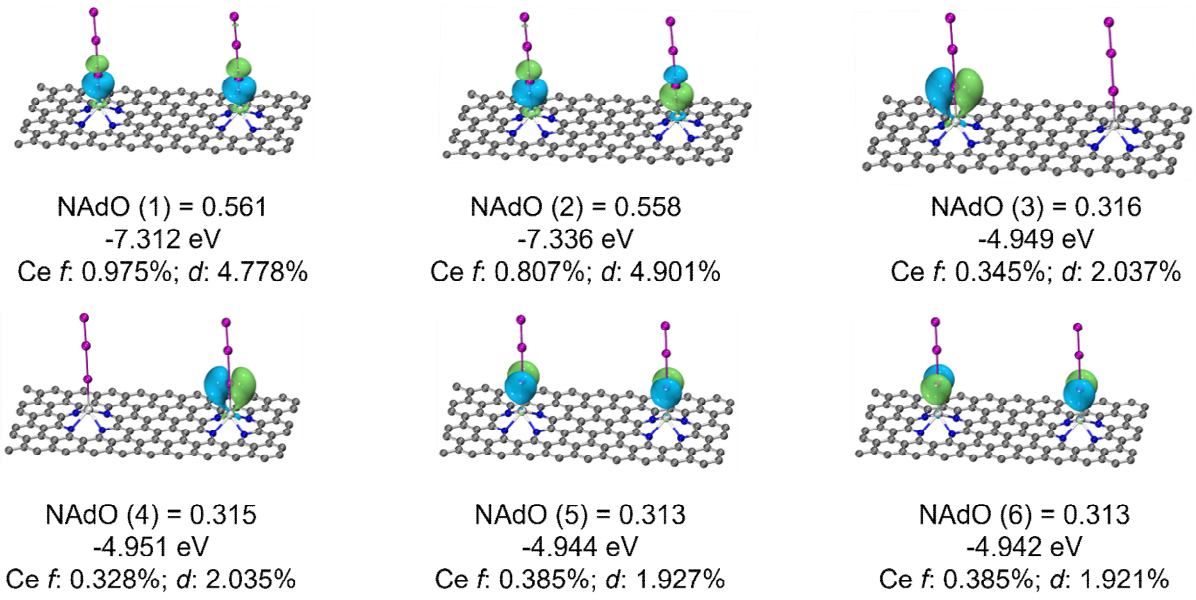


NAdO (5) = 0.431
-5.259 eV
Ce *f*: 1.126%; *d*: 2.715%

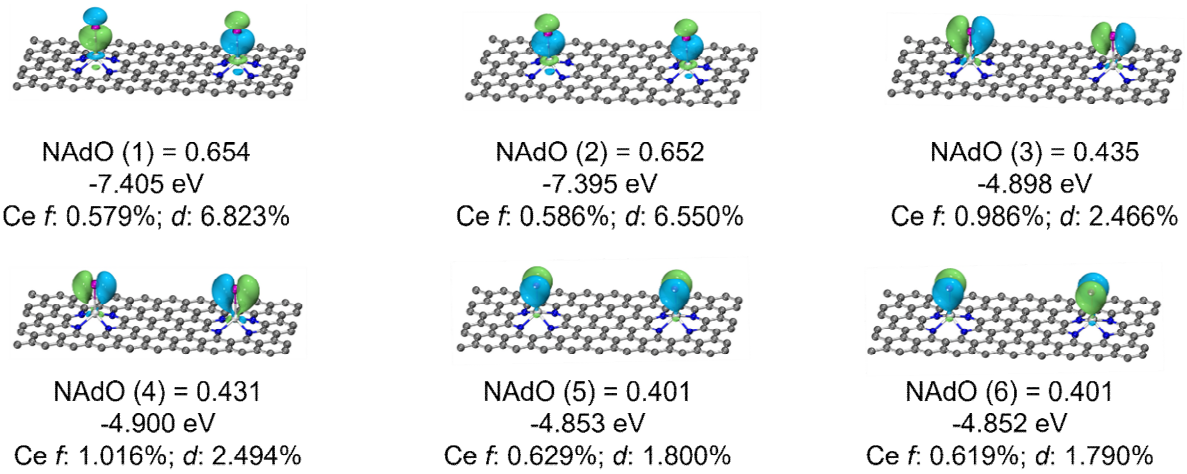


NAdO (6) = 0.430
-5.209 eV
Ce *f*: 0.774%; *d*: 2.069%

Supplementary Fig. 27 | The dominant bonding NAdOs between Ce and I atoms in the adsorbed state of Ce SAC + *I_2. Each orbital is labeled with its bond order contribution (eigenvalue), orbital energy, and the orbital composition in terms of Ce d and f orbitals. The isosurface value is set to 0.03 a.u. Orbitals are displayed in order of decreasing bond order contribution. Blue, purple and gray spheres represent N, I and C atoms, respectively.



Supplementary Fig. 28 | The dominant bonding NAdOs between Ce and I atoms in the adsorbed state of Ce SAC + *I_3. Each orbital is labeled with its bond order contribution (eigenvalue), orbital energy, and the orbital composition in terms of Ce *d* and *f* orbitals. The isosurface value is set to 0.03 a.u. Orbitals are displayed in order of decreasing bond order contribution. Blue, purple and gray spheres represent N, I and C atoms, respectively.



Supplementary Fig. 29 | The dominant bonding NAdOs between Ce and I atoms in the adsorbed state of Ce SAC + *I. Each orbital is labeled with its bond order contribution (eigenvalue), orbital energy, and the orbital composition in terms of Ce *d* and *f* orbitals. The isosurface value is set to 0.03 a.u. Orbitals are displayed in order of decreasing bond order contribution. Blue, purple and gray spheres represent N, I and C atoms, respectively.

Supplementary Note 1

We initiated our investigation by constructing a comprehensive feature space based on representative 3*d*/4*d* transition metal SACs widely explored for Zn||I_2 batteries. The initial descriptors encompassed atomic-scale physicochemical parameters including atomic radius, M–N bond length, and metal center magnetic moment (**Supplementary Figs. 1, 2 and Supplementary Table 2**). To reduce dimensionality and eliminate redundant variables, we first applied Spearman correlation analysis to perform feature pre-screening based on monotonic relevance. This step effectively reduced the feature space to 20 variables while retaining key structure–property relationships. Subsequently, a linear regression model was employed to perform final feature selection and regression fitting, allowing interpretable relationships to be extracted between descriptors and performance indicators.

Given that performance enhancement in Zn||I_2 batteries relies on promoting polyiodide conversion and suppressing the shuttle effect, we introduced two target properties as proxies for catalytic activity: the I–I bond activation length in the rate-determining $*I_3 \rightarrow *I$ step[1] and the adsorption energy of *I (ΔE_{*I}). Density functional theory (DFT) calculations revealed strong linear correlations among the adsorption energies of representative polyiodide intermediates (*I, $*I_2$, $*I_3$), highlighting the potential to unify adsorption trends via a shared descriptor space (**Supplementary Fig. 3a**).

Feature-response analysis revealed that the *d*-orbital electron occupancy (N_d) exhibits a strong positive correlation with the ability to elongate and activate the I–I bond, while the degree of charge transfer between the metal site and its ligands (quantified as ΔBader) governs the adsorption strength of *I. However, due to limited *d–p* orbital overlap in 3*d*/4*d* SACs, it remains challenging to simultaneously optimize both descriptors, revealing a fundamental trade-off between adsorption and activation capabilities. To circumvent this limitation, we expanded the material design space to include 5*d* transition metals and rare-earth elements with accessible 4*f* orbitals. Within this extended space, Ce-based SACs were identified via our ML-augmented DFT workflow as promising candidates capable of achieving both strong *I adsorption and efficient I–I bond activation. The linear regression model yielded high coefficients of determination for both target properties (R^2= 0.81 for ΔE_{*I} and 0.89 for I–I activation), validating the predictive capability of the selected descriptors. Notably, the final composite descriptors—ΔBader – N_f and N_d + N_f—encode the synergistic effects of charge polarization and *d/f* orbital coupling, respectively. These descriptors exhibit no linear correlation (**Fig. 1d**), enabling their independent optimization.

To further quantify site-selectivity under competitive adsorption conditions, we defined a performance index, $\Delta E_{*I}/(\Delta E_{*I3} - \Delta E_{*I})$, representing the relative adsorption preference between *I and $*I_3$ (**Supplementary Fig. 3b**). This ratio closely followed the trend of ΔBader – N_f, reaffirming its effectiveness as a key descriptor. Remarkably, Ce SACs exhibited the highest adsorption ratio, implying minimal energy differences between $*I_3$ and *I adsorption, which could suppress active site poisoning by mitigating competitive adsorption.

Supplementary Table 1 | Adsorption energies of different polyiodide species (*I, *I_2, *I_3).

Materials	ΔE_{*I}	ΔE_{*I2}	ΔE_{*I3}
Co	–3.14323	–3.11748	–3.6868
Cu	–2.44882	–2.61709	–3.03393
Fe	–3.6154	–3.14926	–4.0027
Mo	–5.42272	–5.22825	–5.77151
Nb	–4.48089	–5.81421	–6.16948
V	–4.8542	–4.49819	–5.1984
Zr	–6.82468	–6.32712	–7.15764
W	–5.32321	–5.55954	–5.6741
Ce	–9.1976	–8.65308	–9.52208
La	–7.64305	–6.9794	–8.12013
Sm	–7.25887	–6.54638	–7.70373

Supplementary Table 2 | The description of features used in this study.

Number	Abbreviations	Description
1	Z	The atomic number of M
2	VE	Valence electrons of M
3	M–N1	The bond length of M–N1
4	M–N2	The bond length of M–N2
5	M–N3	The bond length of M–N3
6	M–N4	The bond length of M–N4
7	M–N	The average bond length of M–N
8	N1–M–N2	The bond angle of N1–M–N2
9	N2–M–N3	The bond angle of N2–M–N3
10	N3–M–N4	The bond angle of N3–M–N4
11	N4–M–N1	The bond angle of N4–M–N1
12	ICOHP	ICOHP of M and ligand N
13	ΔBader	*Δ*Bader charge of M
14	Bader	Bader charge of M
15	Nd	Electron occupancy number of *d*-orbital
16	Np	Electron occupancy number of *p*-orbital
17	Ns	Electron occupancy number of *s*-orbital
18	N	Total electron occupancy number
19	χ_m	Ionization energy of M
20	R	Atomic radius of M
21	$\Delta\varepsilon_{dxy}$	Spin center difference of the d_{xy} orbital
22	$\Delta\varepsilon_{dyz}$	Spin center difference of the d_{yz} orbital
23	$\Delta\varepsilon_{dz2}$	Spin center difference of the d_{z2} orbital
24	$\Delta\varepsilon_{dxz}$	Spin center difference of the d_{xz} orbital
25	$\Delta\varepsilon_{dx2-y2}$	Spin center difference of the d_{x2-y2} orbital
26	Δε	Total spin center difference
27	Mag	Magnetic moment of M
28	ε1	Center of the spin-up orbital of M
29	$\varepsilon d1_{xy}$	Center of the spin-up d_{xy} orbital of M

30	$\varepsilon d1_{yz}$	Center of the spin-up d_{yz} orbital of M
31	$\varepsilon d1_{z2}$	Center of the spin-up d_{z2} orbital of M
32	$\varepsilon d1_{xz}$	Center of the spin-up d_{xz} orbital of M
33	$\varepsilon d1_{x2-y2}$	Center of the spin-up d_{x2-y2} orbital of M
34	$\varepsilon 2$	Center of the spin-down orbital of M
35	$\varepsilon d2_{xy}$	Center of the spin-down d_{xy} orbital of M
36	$\varepsilon d2_{yz}$	Center of the spin-down d_{yz} orbital of M
37	$\varepsilon d2_{z2}$	Center of the spin-down d_{z2} orbital of M
38	$\varepsilon d2_{xz}$	Center of the spin-down d_{xz} orbital of M
39	$\varepsilon d2_{x2-y2}$	Center of the spin-down d_{x2-y2} orbital of M
40	$\varepsilon d1$	Center of the spin-up *d* orbital of M
41	$\varepsilon d2$	Center of the spin-down *d* orbital of M

Supplementary Table 3 | Curve fit parameters of Co K-edge EXAFS for Co SACs.

Sample	Path	N	R/(Å)	σ^2/Å^2	ΔE/eV	R factor
Co SACs	Co-N	4.00	1.946	0.015	0.077	0.009

Supplementary Table 4 | Curve fit parameters of Ce K-edge EXAFS for Ce SACs.

Sample	Path	N	R/(Å)	σ^2/Å^2	ΔE/eV	R factor
Ce SACs	Ce-N	4.00	2.021	0.010	-0.100	0.020

Supplementary Table 5 | Fitted R_{ct} values for Zn||I_2 cells with Ce SACs/I_2 and Co SACs/I_2 electrodes at 1.1 V and 1.3 V under different temperatures.

	Temperature	25°C	30°C	35°C	40°C	45°C
Ce SACs (1.3V)	R_{ct} (Ω)	6.11	5.57	4.88	4.52	3.70
	Error(%)	3.69	4.33	4.30	4.34	5.74
Co SACs (1.3V)	R_{ct} (Ω)	19.49	14.87	11.92	10.97	8.92
	Error(%)	2.48	2.75	2.79	2.66	3.05
Ce SACs (1.1V)	R_{ct} (Ω)	0.62	0.42	0.32	0.19	0.14
	Error(%)	3.08	2.84	4.12	4.96	6.54
Co SACs (1.1V)	R_{ct} (Ω)	0.84	0.59	0.40	0.22	0.12
	Error(%)	2.45	2.05	3.79	5.84	6.70

Supplementary Table 6 | The values of descriptor ΔBader – N_f , $N_d + N_f$ and the total descriptor (TD) in different SACs.

Materials	ΔBader − N_f	$N_d + N_f$	TD
Co	–1.17	7.369618	–0.95292
Cu	–0.98	9.160163	–0.90273
Fe	–1.34	6.355251	–1.01839
Mo	–1.94	4.362543	–1.30505
Nb	–1.87	3.233528	–1.22395
V	–1.73	3.544914	–1.15169
Zr	–2.77	2.248662	–1.72408
W	–2.08	0.41538	–1.25006
Ce	–3.48483	2.007067	–2.14024
La	–2.73553	1.80371	–1.68803
Sm	–2.5	2.36488	–1.56777

Supplementary Table 7. Summary of the electrochemical performance of Ce SACs/I_2 in comparison with previous reports, with a focus on mass loading, specific current, areal capacity, capacity retention, and cycling stability.

Positive electrode	Mass loading (mg cm^{-2})	Specific current (A g^{-1})	Areal capacity (mAh cm^{-2})	Capacity retention (%)	Cycling number	References
Ce SACs/I_2	**35**	**0.5**	**6.1**	**96**	**137**	**This work**
	4	**10**	**0.8**	**74**	**31700**	
B-Fe-NC/I_2	1	2.11	0.2	99	10000	2
I_2/PNC-1000	3	0.2	0.7	95	10000	3
PAH-PCH gel	3	1.68	0.3	85.6	18000	4
Fe SAC-MNC/I_2	1.2-1.8	0.5	0.2-0.3	81	50000	5
SACu@NKB	2	0.2	0.4	92	5000	6
I_2/NiSAs-HPC	1	1	0.2	94	10000	7
Carbon cloth/I_2	3.2	20	0.7	90	200	8
I_2/OSTC	1.5-2.5	1	0.3-0.5	85	10000	9
G/PVP@ZnI_2	4.0-5.0	0.2	0.6-0.7	80	1000	10
Starch	3	10	0.2	90	50000	11
CMK-3@I_2	1.2-1.5	0.2	0.2	86	10000	12
Fe-SAs@BNCF/I_2	8.2	1	1.3	80	100	13
Ferrocene/ferrocenium	30.3	0.1	5	95	200	14
NZ-aNC@I_2	5.5	5	0.8	93	1500	15
I_2/CCTF-TPMB	3	5	0.5	93.9	30000	16

Supplementary Table 8 | Calculated Ce–I Mayer bond orders and bond lengths (Å) for iodine species at different reaction stages.

Materials	Ce−I Mayer bond order	Ce−I (Å)
$*I_2$	1.33	2.69651
$*I_3$	0.97	3.0183
*I	1.24	2.73983

Reference

1 Yang, J. *et al.* Theoretical calculation-driven rational screening of d-block single-atom electrocatalysts based on d–p orbital hybridization for durable aqueous zinc–iodine batteries. *Energy Environ. Sci.* **18**, 236-245 (2024).

2 Liu, M. *et al.* Physicochemical confinement effect enables high-performing zinc–iodine batteries. *J.Am.Chem.Soc.* **144**, 21683-21691 (2022).

3 Liu, T. *et al.* Recognition of the catalytic activities of graphitic N for zinc-iodine batteries. *Energy Storage Mater.* **53**, 544-551 (2022).

4 Yang, J.-L. *et al.* Hetero-polyionic hydrogels enable dendrites-free aqueous Zn-I_2 batteries with fast kinetics. *Adv. Mater.* **35**, 2306531 (2023).

5 Yang, X. *et al.* Aqueous zinc batteries with ultra-fast redox kinetics and high iodine utilization enabled by iron single atom catalysts. *Nano-Micro Lett.* **15**, 126 (2023).

6 Yang, F. *et al.* Single atom catalysts for triiodide adsorption and fast conversion to boost the performance of aqueous zinc–iodine batteries. *Energy Environ. Sci.* **16**, 4630-4640 (2023).

7 Ma, L. *et al.* Long-lasting zinc–iodine batteries with ultrahigh areal capacity and boosted rate capability enabled by nickel single-atom electrocatalysts. *Nano Lett.* **23**, 5272-5280 (2023).

8 Li, Y., Liu, L., Li, H., Cheng, F. & Chen, J. Rechargeable aqueous zinc–iodine batteries: pore confining mechanism and flexible device application. *Chem. Commun.* **54**, 6792-6795 (2018).

9 Chen, M. *et al.* Tightly confined iodine in surface-oxidized carbon matrix toward dual-mechanism zinc-iodine batteries. *Energy Storage Mater.* **59**, 102760 (2023).

10 Zhang, Y. *et al.* Iodine promoted ultralow Zn nucleation overpotential and Zn-rich cathode for low-cost, fast-production and high-energy density anode-free Zn-iodine batteries. *Nano-Micro Lett.* **14**, 208 (2022).

11 Zhang, S.-J. *et al.* Polyiodide confinement by starch enables shuttle-free Zn–iodine zatteries. *Adv. Mater.* **34**, 2201716 (2022).

12 Guo, Q. *et al.* In situ synthesis of cathode materials for aqueous high-rate and durable Zn–I_2 batteries. *ACS Mater. Lett.* **4**, 1872-1881 (2022).

13 Li, Y. *et al.* Nano-carbon supported B/N-coordinated Fe single atoms with a tuned electronic structure for long lifespan zinc–iodine batteries. *Energy Environ. Sci.* **18**, 7213-7222 (2025).

14 Zhang, S.-J. *et al.* Electroactive ferrocene/ferrocenium redox coupling for shuttle-free aqueous zinc–iodine pouch cells. *Nat. Chem.* 10.1038/s41557-025-01986-7 (2025).

15 Ye, J., Tian, W., Du, Y. & Ji, J. Defect-engineered ZIF-derived carbon hosts for long-life aqueous zinc-iodine batteries. *Adv. Funct. Mater.* **35**, 2509582 (2025).

16 Zhao, Y. *et al.* Unveiling the role of cationic pyridine sites in covalent triazine framework for boosting zinc–iodine batteries performance. *Adv. Mater.* **36**, 2403097 (2024).